International Journal of Pharmaceutics 554 (2019) 327–336

Contents lists available at ScienceDirect

International Journal of Pharmaceutics

journal homepage: www.elsevier.com/locate/ijpharm

# Designed inorganic porous nanovector with controlled release and MRI features for safe administration of doxorubicin

Simo Näkki[a,b], Julie T.-W. Wang[b], Jianwei Wu[c,d], Li Fan[c,*], Jimi Rantanen[a], Tuomo Nissinen[a], Mikko I. Kettunen[e], Matilda Backholm[f], Robin H.A. Ras[f,g], Khuloud T Al-Jamal[b,*], Vesa-Pekka Lehto[a], Wujun Xu[a,*]

[a] Department of Applied Physics, Faculty of Science and Forestry, University of Eastern Finland, Kuopio 70211, Finland
[b] School of Cancer and Pharmaceutical Sciences, Faculty of Life Sciences & Medicine, King's College London, London SE1 9NH, UK
[c] Department of Pharmaceutical Analysis, School of Pharmacy, and The State Key Laboratory of Cancer Biology (CBSKL), The Fourth Military Medical University, Xi'an, Shaanxi 710032, China
[d] Department of Oncology, Xijing Hospital, The Fourth Military Medical University, Xi'an, Shaanxi 710032, China
[e] A. I. Virtanen Institute for Molecular Science, 70221 Kuopio, Finland
[f] Department of Applied Physics, School of Science, Aalto University, 02150 Espoo, Finland
[g] Department of Bioproducts and Biosystems, School of Chemical Engineering Aalto University, 02150 Espoo, Finland

ARTICLE INFO

*Keywords:*
Porous silicon
Nanoparticle
Cancer therapy
Biocompatibility
Theranostics
Safety

ABSTRACT

The inability of traditional chemotherapeutics to reach cancer tissue reduces the treatment efficacy and leads to adverse effects. A multifunctional nanovector was developed consisting of porous silicon, superparamagnetic iron oxide, calcium carbonate, doxorubicin and polyethylene glycol. The particles integrate magnetic properties with the capacity to retain drug molecules inside the pore matrix at neutral pH to facilitate drug delivery to tumor tissues. The MRI applicability and pH controlled drug release were examined *in vitro* together with in-depth material characterization. The *in vivo* biodistribution and compound safety were verified using A549 lung cancer bearing mice before proceeding to therapeutic experiments using CT26 cancer implanted mice. Loading doxorubicin into the porous nanoparticle negated the adverse side effects encountered after intravenous administration highlighting the particles' excellent biocompatibility. Furthermore, the multifunctional nanovector induced 77% tumor reduction after intratumoral injection. The anti-tumor effect was comparable with that of free doxorubicin but with significantly alleviated unwanted effects. These results demonstrate that the developed porous silicon-based nanoparticles represent promising multifunctional drug delivery vectors for cancer monitoring and therapy.

## 1. Introduction

A non-specific drug distribution is a major limitation of most chemotherapeutic agents, which results in significant toxicity to healthy tissues. Doxorubicin (DOX) is a widely used chemotherapeutic drug to treat various cancers (Lu et al., 2011); although an effective anti-cancer agent, the severe systemic toxicity of DOX in kidneys, liver and heart raises major concerns (Wu et al., 2016). In particular, the dose-dependent cardiotoxicity and the subsequent lethal heart failure are alarming (Takemura and Fujiwara, 2007). Recently, nanotechnology has made possible novel approaches and new treatment options for cancer therapy (Beik et al., 2016; Näkki et al., 2017; Parodi et al., 2013). Nanoparticles have been claimed to improve the delivery of chemotherapeutics, biologics or other therapeutic molecules (Shi et al., 2017). Loading DOX into nanoparticles has been shown to improve the safety and efficiency of the drug by delivering it specifically into the cancer tissues and protecting the drug from premature release and degradation in the blood circulation (Han et al., 2016; Laubrock et al., 2000; Liang et al., 2016). Doxil® represents the first generation of nanomedicines where DOX has been loaded inside a liposome. Doxil® was approved by FDA over two decades ago for the treatment of ovarian cancer, AIDS-related Kaposi's sarcoma and multiple myeloma; it has a prolonged blood circulation time due to its polyethylene glycol (PEG) shielding which reduces some of the unwanted effects as compared with the free drug (Barenholz, 2012). However, Doxil® is still rather simple in its design and does not overcome the main problem related to

* Corresponding authors.
*E-mail addresses:* wujun.xu@uef.fi (W. Xu), khuloud.al-jamal@kcl.ac.uk (K.T. Al-Jamal), xxfanny@fmmu.edu.cn (L. Fan).

https://doi.org/10.1016/j.ijpharm.2018.10.074
Received 24 May 2018; Received in revised form 7 October 2018; Accepted 31 October 2018
Available online 02 November 2018
0378-5173/ © 2018 Elsevier B.V. All rights reserved.

liposomal drug delivery i.e. uncontrolled drug leakage (Russell et al., 2018; Zhang et al., 2015).

Nanotechnology has been explored extensively in recent decades demonstrating an impressive potential in the field of drug delivery. An optimal drug carrier should be able to overcome the body's multiple biological barriers, e.g. the immune system, it should retain the drug molecules before their controlled release in the target and furthermore it should possess a diagnostic potential since this would help to evaluate the efficacy of the treatment. Therefore, the current development of next generation nanomedicines has focused on combining therapeutic and diagnostic features into the same carrier (so-called 'theranostics') with the properties for active targeting and controlled drug release (Janib et al., 2010; Xie et al., 2010). In general, the trend for future nanomedicines seems to involve integrating multiple functionalities into a single carrier (Bao et al., 2013; Cheng et al., 2014; Cole and Holland, 2015; Jia et al., 2013). Nonetheless, no matter how sophisticated the design of the nanoparticle, the safety and the therapeutic efficacy are the two most crucial factors in determining its potential exploitability.

Although there is a broad selection currently being investigated, porous silicon (PSi) has proven to be a promising material. PSi has a large pore volume and thus it has a good drug molecule payload capacity as well as being biocompatible and biodegradable (Park et al., 2009, Tölli et al., 2014). Furthermore, PSi can be easily functionalized even with multiple moieties simultaneously due to the well-known surface chemistry of silicon (Canham, 1995; Näkki et al., 2015; Salonen et al., 2008). Previously, we have developed a tailored coating method for PSi where two PEGs (Dual PEGylation) with different molecular weights have been simultaneously incorporated to improve the *in vitro* and *in vivo* colloidal stability and behavior (Näkki et al., 2015; Nissinen et al., 2016). In the present paper, we report a further development of the PSi nanoparticles to make them more suitable for cancer theranostics. Our novel nanovectors are composed of a PSi core loaded with the chemotherapeutic drug, DOX, and surrounded with superparamagnetic iron oxide nanoparticles (SPIONs) with good magnetic resonance imaging (MRI) properties. Finally, the composite is coated with a pH-sensitive $CaCO_3$ layer and shielded with Dual PEGylation (Scheme 1). Nanoparticles suitable for imaging were manufactured with an identical protocol except there was no loading of DOX, instead a third PEG-molecule (Triple-PEGylation, TPEGylation) with an amine group was included to allow conjugation with a fluorescent dye (Scheme 1). Even though pH-sensitive $CaCO_3$ has been used as a drug carrier before (Liang et al., 2013; Wei et al., 2008), as far as we are aware, there are no studies which have investigated $CaCO_3$ as a pH-sensitive gate-keeper to control drug release from porous nanocarriers. Moreover, therapeutic outcomes with these $CaCO_3$-based drug delivery systems have been rarely verified in *in vivo* animal experiments (Liu et al., 2017; Zhao et al., 2018). In the present study, the developed nanovectors exhibited pH controlled drug release, a good *in vitro* therapeutic effect and minimal *in vivo* toxicity in healthy tissues after systemic administration. Furthermore, the nanovectors achieved an excellent therapeutic effect *in vivo* after intratumoral injection.

## 2. Materials and methods

### 2.1. Materials

Triethylene glycol (TEG), iron(III) acetylacetonate ($Fe(acac)_3$), Igepal Co-520 (IGE), calcium chloride ($CaCl_2$), sodium carbonate ($Na_2CO_3$), (3-Aminopropyl)triethoxysilane (APTES), trimethylamine (TEA), fetal bovine serum (FBS), Tween® 20 and L-glutamine were purchased from Sigma-Aldrich. Doxorubicin (DOX) was purchased from Euroasias. Cyclohexane (CH) and tetramethoxysilane (TMOS) were obtained from Merck Millipore and Alfa Aesar, respectively. Dimethyl sulfoxide was purchased from J.T. Baker. 2 kDa PEG-silanes (mPEG & $NH_2$) and 0.5 kDa mPEG-silane were purchased from Huateng Pharma and Fluorochem, respectively. Cyanide7.5 NHS ester (Cy7.5) and CellTiter-Glo were purchased from Lumiprobe and Promega, respectively. Dulbecco's Modified Eagle Medium (DMEM) and RPMI1640 were obtained from Biowest and penicillin/streptomycin (P/S) was

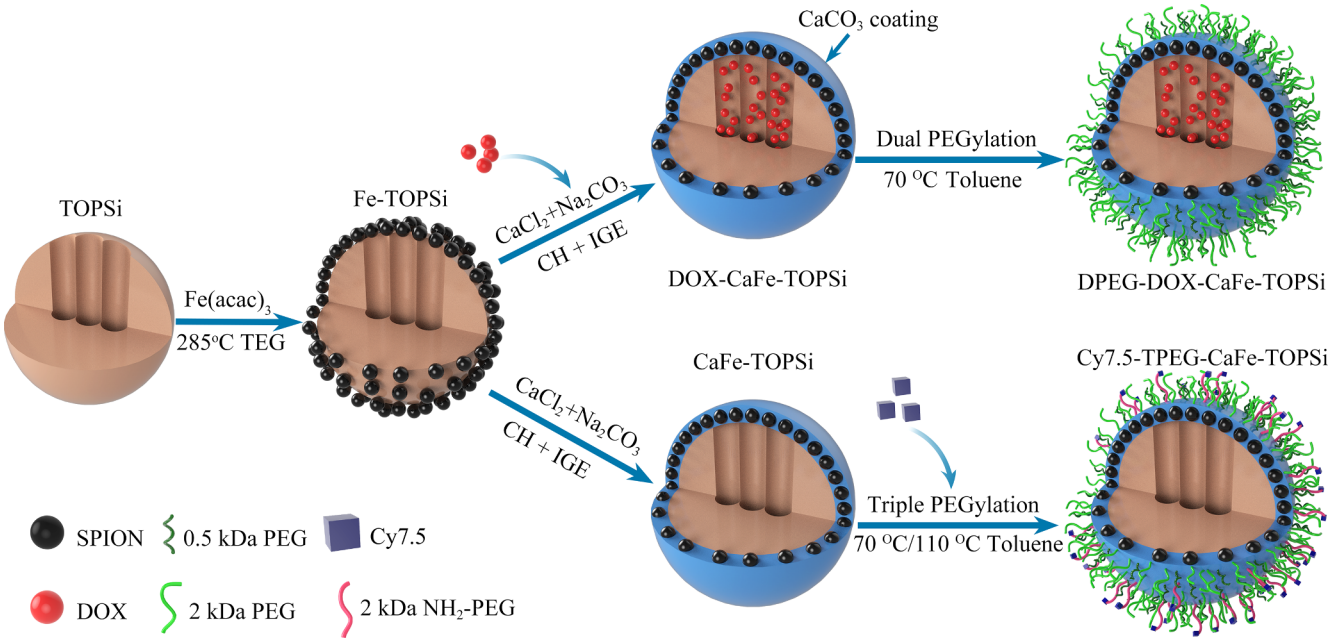


**Scheme 1.** Schematic illustration of particle modification routes. Oxidized PSi (TOPSi) nanoparticles are immersed in triethylene glycol (TEG) with iron(III) acetylacetonate ($Fe(acac)_3$) and heated to produce SPIONs on the surface of TOPSi (Fe-TOPSi). DOX is loaded in the pores of the Fe-TOPSi nanoparticles and calcium carbonate coating is conducted in cyclohexane (CH):Igepal Co-520 (IGE) solution (DOX-CaFe-TOPSi). Dual PEGylation is applied in toluene to shield the nanoparticles with PEG (DPEG-DOX-CaFe-TOPSi). A similar protocol without DOX is utilized to manufacture particles for fluorescent imaging with the exception of the addition of extra PEG molecules with an amine group on the shielding step and labeling with Cy7.5 in the final step (Cy7.5-TPEG-CaFe-TOPSi).

purchased from Hyclone. Alexa Fluor546, CellMask Deep Red, and Hoechst stain were purchased from Thermo Scientific. Silicon wafers ($p^+$-type, resistivity 0.007–0.02 Ωcm) were received from Okmetic Oyj.

### 2.2. Synthesis of DPEG-DOX-CaFe-TOPSi

PSi was prepared by electrochemical pulsed etching (30 mA/cm$^2$ for 2200 ms and 120 mA/cm$^2$ for 350 ms, total etching time 40 min) in a 1:1 mixture of hydrofluoric acid and ethanol followed by milling and centrifugation to obtain nanoparticles (NPs). The PSi NP surface was oxidized thermally and chemically according to the previous protocol for the preparation of oxidized PSi (TOPSi) (Näkki et al., 2015). SPIONs were deposited on the surface of TOPSi nanoparticles with $Fe(acac)_3$. Briefly, TOPSi and $Fe(acac)_3$ (1:1 ratio) were dispersed in TEG, heated at 275 °C for 30 min, cooled down to room temperature (RT) and washed with ethanol (EtOH) to obtain SPION decorated TOPSi (Fe-TOPSi). Fe-TOPSi NPs (30 mg) were immersed in DOX (30 mg/ml in 1:1 v/v EtOH:$H_2O$, 0.5 ml) solution to load the drug into the pores (DOX-Fe-TOPSi). DOX-Fe-TOPSi were coated with a pH-sensitive $CaCO_3$ layer by a microemulsion method. Briefly, DOX-Fe-TOPSi nanoparticles in the DOX loading (0.5 ml) solution were dispersed in CH:IGE mixture (volumes of 5 and 1.5 ml, respectively) with the aid of ultrasound. $CaCl_2$ (200 µl ($H_2O$), 0.5 M) was mixed with a similar CH:IGE mixture. The solutions of DOX-Fe-TOPSi and $CaCl_2$ were mixed with sonication and stirred for 5 h at RT to obtain a microemulsion. $Na_2CO_3$ (200 µl ($H_2O$), 0.5 M) was added into a similar CH:IGE mixture, subsequently mixed by sonication with the microemulsion, and stirred overnight at RT to obtain DOX-CaFe-TOPSi nanoparticles which still remained in the solution.

30 µl APTES and 30 µl TMOS were mixed with CH (2 ml), added to DOX-CaFe-TOPSi particle solution and reacted for 5 h at RT before washing with EtOH. The previously described Dual PEGylation (Näkki et al., 2015) was performed at lower temperatures (max 70 °C) to ensure the integrity of DOX. The final particles were denoted as DPEG-DOX-CaFe-TOPSi. A similar production protocol without DOX was utilized to manufacture unloaded DPEG-CaFe-TOPSi. Particles with a reactive group for dye labelling were manufactured with a similar protocol without DOX by including an extra PEGylation step before the final Dual PEGylation; The CaFe-TOPSi particles were PEGylated in toluene with $NH_2$-PEG-silane at 70 °C overnight before Dual PEGylation to manufacture TPEG-CaFe-TOPSi.

### 2.3. Characterization

Fourier-transform infrared spectroscopy (FTIR, Thermo Nicolet 8700) was utilized to monitor the chemical changes after modifications by measuring total transmittance. Nanoparticle size and morphology were imaged with transmission electron microscopy (TEM, Jeol JEM 2100F) after drying a droplet of NP suspension onto a copper grid and imaging with 200 kV. The iron and $CaCO_3$ contents were measured with atomic absorption spectroscopy (AAS, Jena AAS ZEEnit 700) by using 248.3 nm and 422.7 nm wavelengths for iron and calcium, respectively. Thermogravimetric analysis (TGA, TA Instruments TG Q50) was utilized to measure PEG content by ramping the temperature at 20 °C/min intervals up to 800 °C in an $N_2$ atmosphere. Ultra-visible absorption (480 nm) (UV–Vis, PerkinElmer Victor 3) was used for analyzing the amount of DOX released. Pore properties were measured from dry particles with $N_2$ sorption (Micromeritics TriStar II 3020) at -196 °C. Specific surface areas were calculated using the Brunauer–Emmet–Teller (BET) method, and a single point method ($p/p_0 = 0.95$) was used to obtain the pore volumes. Average pore sizes were calculated from the desorption branch using the Barrett–Joyner–Halenda (BJH) theory. X-ray powder diffraction (XRPD) (Bruker D8 Discover) was utilized to measure SPION and $CaCO_3$ crystalline size with the Scherrer equation after full profile fitting. Magnetization was studied with a vibrating sample magnetometer (VSM, Physical Property Measurement System Dynacool, Quantum Design) equipped with a 9 T magnet. Magnetic relaxation was evaluated with a 9.4 T vertical magnet (Oxford Instruments) interfaced to the Varian DirectDrive console (Agilent Technologies). The particle size and stability in PBS and plasma were measured with dynamic light scattering (Malvern, Nano ZS Zetasizer).

### 2.4. Drug release

DOX release from DPEG-DOX-CaFe-TOPSi NPs (~ 1,5 mg) was determined in an Eppendorf tube at pH 5, 6.5 & 7 buffer. Nanovectors were dispersed in medium with ultrasound (~5 s) and rotated (24 rpm) at 37 °C. At predefined time points, the nanovectors were centrifuged, the medium was collected for analysis and it was replaced with fresh buffer. All samples were analyzed with UV–Vis.

### 2.5. In vitro cell experiments

The therapeutic effect was evaluated with three cancer cell lines; CT26 colon, 4 T1 breast and A549 lung cancer. The cells were cultured in DMEM (A549) or RPMI1640 (CT26 & 4 T1) supplemented with 10% FBS, 1% P/S and 1% L-glutamine. Cells were plated onto a 96-well plate (15 000/cm$^3$) and incubated with DOX, DPEG-DOX-CaFe-TOPSi or DPEG-CaFe-TOPSi for 24 h. The cells were washed twice with PBS and fresh medium was replaced. The cell viability was measured with CellTiter-Glo assay after an additional 24 h incubation based on the manufacturer's instructions. Untreated cells and cells incubated with 10% Tween® 20 were used as controls. The results are normalized to untreated cells (100%) and to Tween® 20 treated cells (0%).

The cell internalization of TPEG-CaFe-TOPSi nanoparticles was evaluated with RAW 264.7 cells cultured in DMEM supplemented with 10% FBS, 1% P/S and 1% L-glutamine. The DOX amount in the cell cytoplasm after incubation with DPEG-DOX-CaFe-TOPSi nanoparticles was examined in CT26 cells. Cells were plated in Ibidi 8-well plate (50 000/cm$^2$) and incubated with Alexa Fluor546-labelled TPEG-CaFe-TOPSi (RAW 264.7) or DPEG-DOX-CaFe-TOPSi (CT26) for 4 and 24 h. The cell membranes were stained with CellMask (1 µg/ml, 7 min) and nuclei with Hoechst (1 µg/ml, 7 min) staining before imaging with confocal microscope (Zeiss, LMS700).

### 2.6. In vivo biodistribution

*In vivo* biodistribution and safety evaluation studies were performed under the authority of project and personal licences granted by the UK Home Office and the UKCCCR Guidelines (1998). Male NOD SCID gamma (NSG) mice (~20 g) aged 4–6 weeks were obtained from Charles River (UK).

TPEG-CaFe-TOPSi were incubated with Cy7.5 dye (59 µM) and TEA (0.2 M) in DMSO (1 ml) overnight at RT under constant shaking. The excess dye was washed away with EtOH and the particles were reconstituted in PBS. Male NSG mice were intravenously (i.v.) injected (tail vein) with Cy7.5-TPEG-CaFe-TOPSi (2.5 mg, with average particle size of ~250 nm) or Cy7.5-TOPSi (1 mg, with average particle size of ~250 nm) with matched fluorescent intensity. The mice were sacrificed at 4 h post injection (p.i.), and organs were collected and imaged with IVIS Lumina III *in vivo* imaging system (PerkinElmer). Free Cy7.5 dye dispersed in PBS (29 µM, 200 µl) was i.v. injected into male NSG mouse, sacrificed 4 h p.i. and organs imaged with IVIS. Biodistribution values are presented as % dose in each organ as compared to the total detected intensity.

### 2.7. In vivo safety evaluation with orthotopic cancer

A549 lung cancer models were established by i.v. injection of luciferase expressing A549-luc cancer cells ($0.5 \times 10^6$) into male NSG mice. The cancer growth was evaluated after subcutaneous injection of

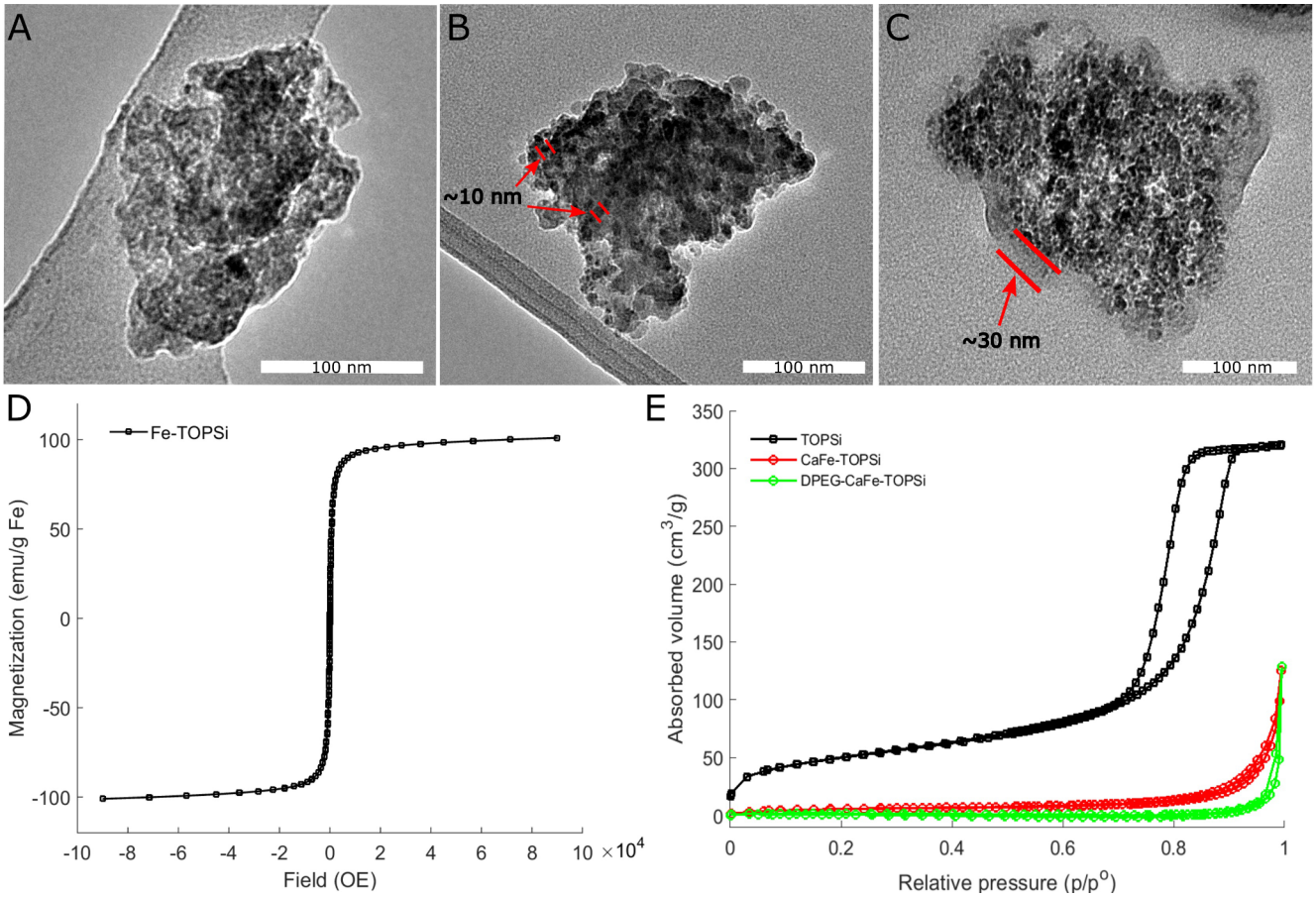


**Fig. 1.** TEM images of A) TOPSi B) Fe-TOPSi with 10 nm SPIONs on the surface and C) CaFe-TOPSi with visible $CaCO_3$ layer of 30 nm. The scale bar is 100 nm. D) The saturation magnetization of Fe-TOPSi was evaluated with VSM, with a value of 100.7 emu/$g_{Fe}$ being obtained. E) Nitrogen sorption results for TOPSi, CaFe-TOPSi and DPEG-CaFe-TOPSi indicative of the pore blocking induced by the $CaCO_3$-layer.

luciferin (150 mg/kg) through bioluminescence imaging (BLI) with IVIS starting from day 7 post cancer cell inoculation. Based on the BLI signals, the mice were divided into four groups (Control, DOX, DPEG-CaFe-TOPSi or DPEG-DOX-CaFe-TOPSi, n = 7) to match signal mean and S.D. between the groups as closely as possible. Each group received weekly i.v. injection of either PBS, free DOX (5 mg/kg), DPEG-CaFe-TOPSi (50 mg/kg, ~250 nm, Table S1) or DOX-DPEG-CaFe-TOPSi (50 gm/kg, DOX equivalent 5 mg/kg, ~250 nm) until they were sacrificed. The mice were monitored for up to 45 days unless they exhibited symptoms or displayed a 20% weight loss as compared to initial weight. At sacrifice, blood samples were collected and major organs were excised, weighed, and fixed for histopathological analysis.

### 2.8. In vivo therapy evaluation with subcutaneous cancer model

*In vivo* animal therapy experiments were approved by the Animal Experiment Administration Committee of the Fourth Military Medical University, China. CT26 cells ($5 \times 10^6$ cells) were injected into female BALB/c nude mice legs subcutaneously in order to establish tumors. Tumor growth was measured with calipers and upon reaching a diameter greater than 0.2 cm, the mice were randomly divided into four groups and given a single intratumoral injection of PBS, DOX (5 mg/kg), DPEG-CaFe-TOPSi (50 mg/kg, 250 nm) or DPEG-DOX-CaFe-TOPSi (50 mg/kg, DOX equivalent of 5 mg/kg, 250 nm). All animals were monitored for activity, physical condition, body weight, and tumor growth until sacrificed at day 10 post treatment. The tumor volume was calculated with the formula V = ½ (width$^2$·length). The excised tumors were weighed and imaged, furthermore the major organs were collected for further analysis.

### 2.9. Histology and blood biochemistry

Heart, A549 lung, liver, spleen and kidney specimens from the *in vivo* safety experiment were fixed and stained with hematoxylin and eosin (H&E). Similarly, the major organs (heart, lung, liver, spleen and kidney as well as the tumor) from *in vivo* therapy experiment were prepared and H&E stained. Furthermore, the tumors were stained with the TUNEL assay to determine the numbers of apoptotic cells in the tumor sections. H&E stained slices were imaged with light microscopy to evaluate the toxicity of each treatment. Serum was extracted from the drained blood by centrifugation and analyzed for alanine aminotransferase (ALT), aspartate aminotransferase (AST), alkaline phosphatase (ALP), blood urea nitrogen (BUN) and creatine kinase (CK) enzymes.

## 3. Results and discussion

The morphology of TOPSi, Fe-TOPSi and CaFe-TOPSi nanoparticles was studied with TEM imaging; the particles had irregular elongated or roundish shapes. Furthermore, TEM revealed 10 nm sized SPIONs on the surface of Fe-TOPSi, and a 30 nm layer of $CaCO_3$ was observed on the surface of CaFe-TOPSi which was not present in TOPSi (Fig. 1A–C).

**Table 1**
The porous and magnetic properties of porous silicon.

| Sample | Surface area[a] ($m^2$/g) | Pore volume[b] ($cm^3$/g) | Pore size (nm)[c] | $T_2$-relaxivity[d] (ml/mg·s) |
|---|---|---|---|---|
| TOPSi | 190 ± 20 | 0.50 ± 0.04 | 9.9 ± 0.2 | – |
| CaFe-TOPSi | 20 ± 2 | 0.07 ± 0.01 | 43 ± 6* | 520 ± 20 |
| DPEG-CaFe-TOPSi | 6 ± 2 | 0.03 ± 0.02 | 42 ± 6* | 186 ± 5 |

[a] Surface area of the samples calculated according to BET theory from $N_2$ sorption isotherms (mean ± S.D., n = 3).
[b] Pore volume of the samples calculated with single-point approximation ($p/p_0$ = 0.95) from $N_2$ sorption isotherms (mean ± S.D., n = 3).
[c] Pore sizes calculated with the BJH theory from $N_2$ sorption isotherms (mean ± S.D., n = 3).
[d] $T_2$-relaxivity (with least squares fitting error).
* The value corresponds to the inter-particle cavities rather than the real pore size.

The nanoparticles were then studied with XRPD (Fig. S1) from which a crystallite size of $Fe_3O_4$ of 3.5 ± 0.1 nm as calculated with the Scherrer equation after full profile fitting. The obtained crystallite size of $CaCO_3$ (33.5 ± 1.1 nm) matched well with the thickness evaluated by TEM. Furthermore, the mean amount of $Fe_3O_4$ was 9 wt% and the $CaCO_3$ amount was 22 wt% as evaluated with AAS.

The CaFe-TOPSi nanoparticles displayed magnetic behavior in the presence of a permanent magnet (Fig. S2) and magnetic performance was further validated with VSM and MRI. The superparamagnetic saturation magnetization from Fe-TOPSi was 100.7 emu/$g_{Fe}$ (Fig. 1D), and the $T_2$-relaxivity of CaFe-TOPSi was 520 ± 20 ml/(mg·s) compared to the total particle mass (Table 1). The DPEGylation decreased the $T_2$-relaxivity to 186 ± 5 ml/(mg·s) on DPEG-CaFe-TOPSi due to impaired water flow near to the particle surface (Nissinen et al., 2016). The obtained values highlight the good magnetic performance for MRI diagnostics and as far as we are aware, this magnetization value is one the highest ever reported for magnetic PSi (Kinsella et al., 2011; Xia et al., 2017).

Tumor tissues have a lower pH (6.5–7) in comparison to normal tissue (Gallagher et al., 2008; Sun et al., 2016); this is anticipated to trigger the pH-sensitive drug release from DPEG-DOX-CaFe-TOPSi. The $CaCO_3$ is practically insoluble at neutral pH and thus blocks the pores in a neutral environment like the bloodstream and therefore protects the drug from premature release in blood and minimizes the absorption of the drug by healthy tissues. The $CaCO_3$ dissolves better in acidic conditions, and this enhances the drug release in the tumor environment (Liu et al., 2017). The pore blocking by $CaCO_3$ was studied with $N_2$ sorption; this revealed the clear differences between CaFe-TOPSi and TOPSi (Fig. 1E). The hysteresis between adsorption and desorption isotherms is related to mesoporosity and non-porous materials do not display this phenomenon whereas the isotherm height is related to the total pore volume. The surface area and pore volume, calculated with BET and single point approximation ($p/p_0$ = 0.95) respectively, decreased by 90% and 86% due to the $CaCO_3$ coating, respectively (Table 1). The obtained large pore size in CaFe-TOPSi and DPEG-CaFe-TOPSi is anticipated to be due to the inter-particle cavities instead of the pores within the sample, since the starting material (TOPSi) had a narrow pore size distribution between 5 and 20 nm whereas there was a wide distribution of the CaFe-TOPSi pores, ranging up to 80 nm (Fig. S3). The lack of the pores with diameters below 20 nm, which are a normal characteristic of a PSi material, emphasizes that $CaCO_3$ exerts a pore blocking effect. FTIR showed characteristic peaks of $CaCO_3$ (Fig. S4) indicating successful coating, and the total PEG content was 15.2 ± 0.8 wt% based on TGA (Fig. S5).

Since the biological stability of the nanoparticles is a critical factor of a good drug carrier, the size changes of DPEG-CaFe-TOPSi in PBS and plasma were evaluated as a function of the incubation time (Figs. 2A and B and S6). The negligible changes in size in both physiological conditions are evidence of the improved and long-term colloidal stability after DPEGylation. The pH sensitive drug release from DPEG-DOX-CaFe-TOPSi was evaluated by measuring DOX release kinetics *in vitro* at three different pH levels (pH 5, 6.5 & 7). The drug release was in good agreement with our hypothesis since the DOX release was clearly inhibited at pH 7, it was moderate at pH 6.5 and the release was extensive at pH 5 (Fig. 2C). The difference in drug release was proposed to be mainly due to $CaCO_3$ since free DOX was seen to rapidly dissolve at pH 5 and 7 buffers (Fig. S7). The total amount of DOX in DPEG-DOX-CaFe-TOPSi, evaluated from the released drug amount with UV–VIS, was 10.3 ± 1.4 wt% (Fig. S9). Furthermore, TGA results (Fig. S5) indicate that the DOX content was 9.2 ± 1.1 wt%, correlating well with the value obtained from the UV–VIS analysis.

The *in vitro* therapeutic effect was studied with CT26, 4 T1 and A549 cell lines in order to gain a more comprehensive understanding of the feasibility of using DPEG-DOX-CaFe-TOPSi for cancer therapy. While DPEG-CaFe-TOPSi displayed excellent biocompatibility (Fig. S10–12), the DPEG-DOX-CaFe-TOPSi revealed evidence of dose-dependent cytotoxicity similar to free DOX (Fig. 2D–F). In general, the DPEG-DOX-CaFe-TOPSi exhibited a slight reduction in cytotoxicity as compared to free DOX. This phenomenon is frequently observed with nanoparticles (Liu et al., 2016; Zhang et al., 2014) and can be related to the controlled release of the drug molecules. Moreover, based on the confocal microscopy examination, the PEG layer seemed to hinder and delay the cell uptake of the particles (Fig. S13). This affected the release and overall content of DOX in the cells (Fig. S14) whereas free DOX could enter the cells via passive diffusion and interact more rapidly with the cells. This may account for the differences detected in the cytotoxicity of these particles. Furthermore, the cell lines responded differently to treatment with DOX and DPEG-DOX-CaFe-TOPSi; the 4 T1 cell line was the most sensitive, the CT26 cell line displayed the lowest therapeutic response (Figs. S15 and S16).

The *in vivo* biodistribution in healthy male NSG mice was evaluated 4 h after intravenous administration of shielded Cy7.5-dye labelled TPEG-CaFe-TOPSi nanoparticles and compared with bare Cy7.5-TOPSi nanoparticles. The TPEG-CaFe-TOPSi particles accumulated significantly less in liver, lungs and kidneys, and more in spleen as compared with the non-PEGylated counterpart (Fig. 3A). The high lung uptake of TOPSi can be related to its poor stability in biological fluids (Fig. 2A and B). The rapid aggregation of the TOPSi nanoparticles leads to their entrapment in the small capillaries of the lungs while TPEG-CaFe-TOPSi nanoparticles were able to maintain their original size and become distributed in other tissues. TOPSi nanoparticles accumulated mainly in liver which is usually the main organ which takes up and removes nanoparticles from the bloodstream (Rytkönen et al., 2012; Wang et al., 2016). The PEGylated nanoparticles however accumulated mostly in the spleen; this can be attributed to the shielding effect of PEG and the changed ζ-potential (Table S2). PEGylation affects the

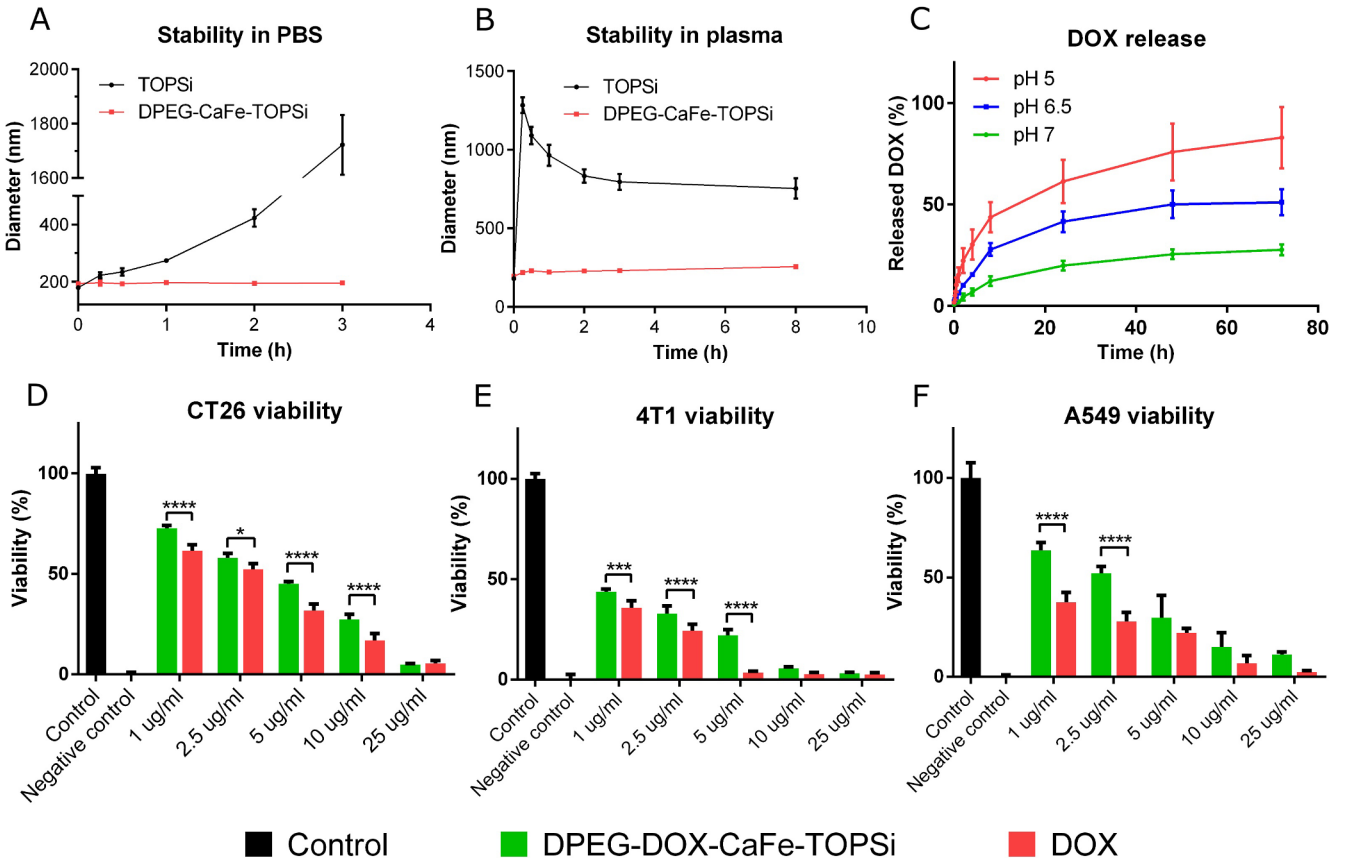


**Fig. 2.** The colloidal stability of TOPSi and DPEG-CaFe-TOPSi in A) PBS and B) plasma reflecting the increased stability of DPEG-CaFe-TOPSi. C) DOX release from nanovectors in pH 5, 6.5 and 7 buffers showing capability of DPEG-DOX-CaFe-TOPSi for achieving pH sensitive drug release. D) CT26, E) 4T1 and F) A549 cancer cell viability after 24 h incubation with DOX or DPEG-DOX-CaFe-TOPSi with equivalent DOX doses. Cell viability was evaluated from luminescence with the CellTiter Glo assay. All results are presented as mean ± S.D. ($n \geq 3$). Significant differences were examined with two-way ANOVA followed by Sidak's test (*$p < 0.05$, ***$p < 0.001$, ****$p < 0.0001$).

opsonized protein corona not only by decreasing the total amount of protein being absorbed but also by altering the nature of these proteins, leading to a "stealth" effect, an increased blood half-time and a different biofate (Nissinen et al., 2016). Furthermore, long blood residence times together with high spleen accumulation have been reported (He et al., 2011; Kramer et al., 2017) indicating that there could be a possible correlation between these two factors. The DPEGylation significantly decreased the signal from the kidneys. This can be related to the small Cy7.5 molecule being excreted out of the bloodstream through the kidneys after being detached from the nanoparticles after their degradation. The DPEGylation slows down the particle degradation as compared with the non-modified particles (Näkki et al., 2015) affecting the amount of free Cy7.5 in the blood. Moreover, the free Cy7.5 after i.v. administration is mainly accumulated in the kidneys corroborating this hypothesis (Fig. S17). Overall, the biodistribution data suggest that DPEGylation had improved the pharmacokinetics of the particles in the blood.

The safety of the developed nanovectors was evaluated in male NSG mice which had been inoculated with luciferase expressing lung cancer A549 cells. The weight and behavior of the mice were monitored starting from the day of tumor inoculation until day 45 post-inoculation when the experiment was terminated. The tumor growth was monitored by whole body BLI imaging after administration of luciferin. Each group received weekly treatment with either PBS (Control), DOX, DPEG-CaFe-TOPSi or DPEG-DOX-CaFe-TOPSi starting from day 7 post-tumor cell inoculation. The DOX dose in the drug-treated groups was 5 $mg \cdot kg^{-1}$/treatment with the corresponding particle amount being 50 $mg \cdot kg^{-1}$/treatment. The mice in the DOX group started to lose weight soon after receiving the first treatment due to the toxicity of the cytostatic drug (Fig. 3B) and they had to be sacrificed on days 17–18 after losing more than 20% of their body weight as compared to the starting situation. Furthermore, the mice in the DOX group displayed abnormal behavior with an untidy appearance and they appeared to have small eyes.

On the contrary, no weight loss or other symptoms were observed in the other groups including the control group. At the end of the experiment, blood was sampled and major organs i.e. heart, lung, liver, spleen and kidney were excised. It was found that many organs in the DOX group were significantly smaller than the corresponding organs in the other groups (Fig. S18). The DOX toxicity was unexpected since the 5 $mg \cdot kg^{-1}$ dose (Wang et al., 2016) is commonly used and even doses as high as 18 $mg \cdot kg^{-1}$ have been administered to mice without any significant toxicity (Cai et al., 2015). Furthermore, the maximum tolerance level for DOX has been reported to be 8 $mg \cdot kg^{-1}$ whereas the loading to nanoparticles can elevate this up to 40 $mg \cdot kg^{-1}$ (Yang et al., 2016). The reduced drug tolerance may be due to the nature of NSG mice which are one of the most immunodeficient mouse strains (Shultz et al., 2007). Surprisingly, the tumors in DOX and DPEG-DOX-CaFe-TOPSi groups did not show any regression, in fact even the opposite effect was encountered in the DOX group where the tumors were significantly larger than in the other groups (day 17) (Fig. 3C). We have been unable to find any other reports of a similar effect after

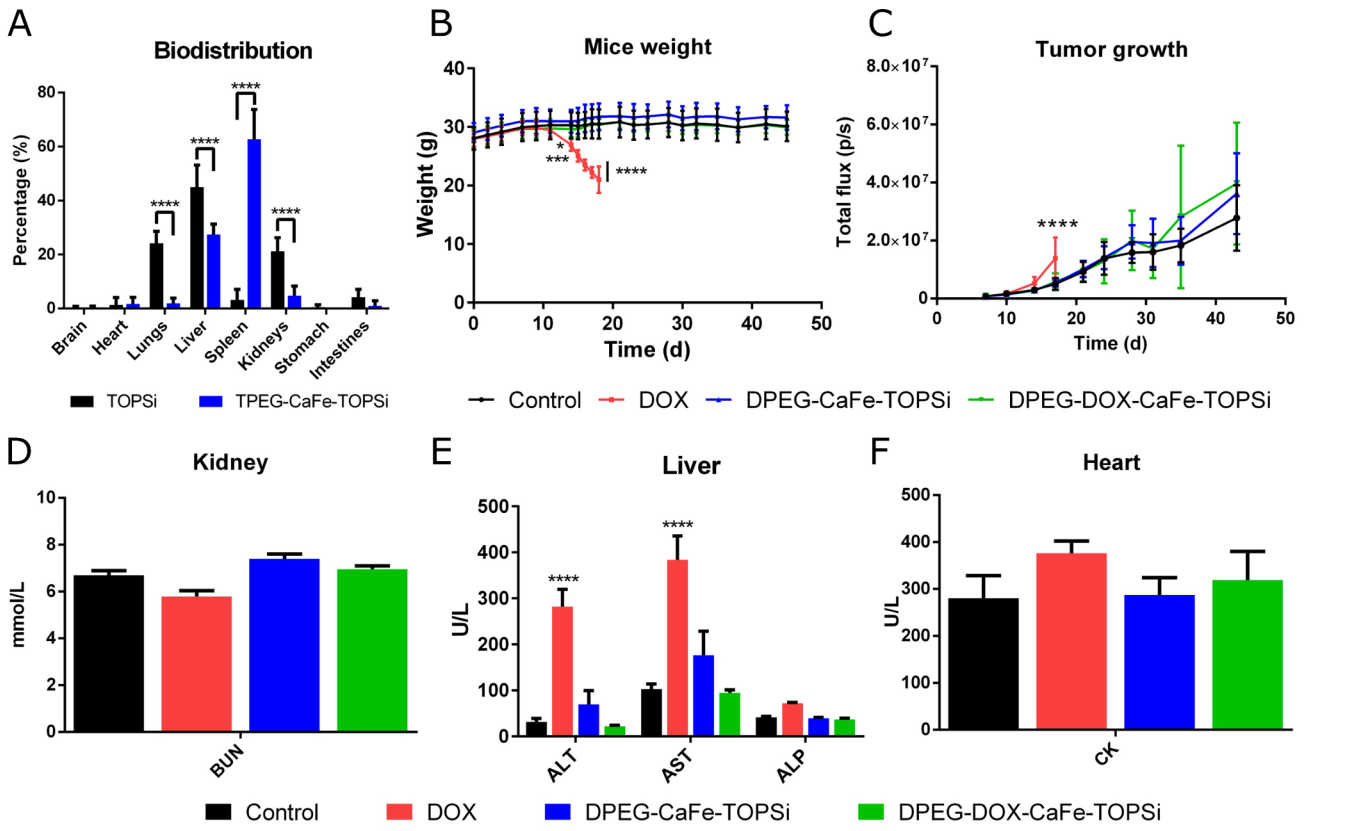


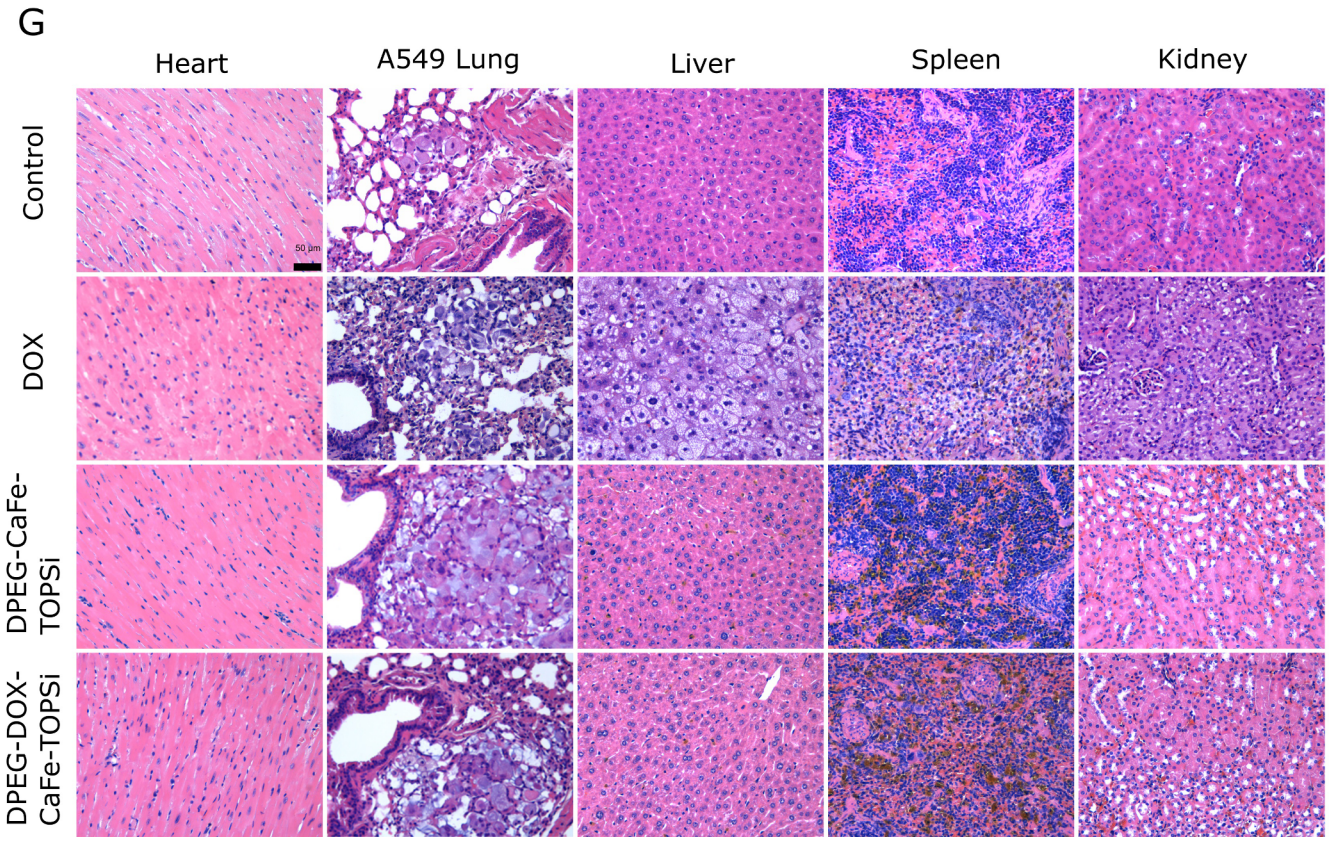


*(caption on next page)*

**Fig. 3.** A) Biodistribution of the Cy7.5 labelled TOPSi and TPEG-CaFe-TOPSi in healthy mice at 4 h post-injection presenting organ distribution scaled to the total detected intensity measured *ex vivo* with IVIS. B) Animal weight during i.v. treatment with PBS (Control), DOX (5 mg/kg), DPEG-CaFe-TOPSi (50 mg/kg) or DPEG-DOX-CaFe-TOPSi (50 mg/kg, DOX equivalent 5 mg/kg) in A549 lung tumor bearing mice. Tumors were inoculated at 0 d and treatments were given once a week starting at day 7 post-inoculation. The animals in the DOX group were sacrificed at 17–18 d post tumor inoculation and received two treatments while other groups were sacrificed at 45 d post tumor inoculation and received six treatments. C) The A549 lung tumor size which was evaluated from the bioluminescence signal arising from the tumor after administration of luciferin. The evaluation of blood biochemical parameters of D) kidney enzyme BUN, E) liver enzymes ALT, AST and ALP, and F) heart enzyme CK from PBS (Control), DOX, DPEG-CaFe-TOPSi and DPEG-DOX-CaFe-TOPSi treated mice. G) Histological examination of vital organs with H&E staining. Scale bar, 50 μm. Results are presented as mean ± S.D. ($n \geq 3$). Significant differences (compared to control group (black)) were examined with two-way ANOVA followed by Sidak's test (*$p < 0.05$, ***$p < 0.001$, ****$p < 0.0001$).

administration of DOX. We hypothesize that it is attributable to the severe toxicity of DOX weakening the animals such that they were not able resist the tumor growth as effectively as their counterparts in the other groups.

Histopathological changes and several biomarkers were examined to determine in detail the toxicity in the vital organs. Blood urea nitrogen (BUN) levels were found to be slightly but not significantly elevated in DPEG-CaFe-TOPSi and DPEG-DOX-CaFe-TOPSi groups indicating no nephrotoxicity had occurred in these groups (Fig. 3D). On other hand, the liver enzyme levels (ALT & AST) were significantly elevated in the DOX group as compared to the control group, i.e. evidence of hepatotoxicity (Fig. 3E). No significant increases in liver enzymes were found in DPEG-CaFe-TOPSi and DPEG-DOX-CaFe-TOPSi groups as compared to the control group. Although DOX is known to possess cardiotoxic properties (Takemura and Fujiwara, 2007), there was no major elevation of the creatine kinase (CK) levels in any of the treatment groups (Fig. 3F). Images of representative H&E stained tissues from vital organs are shown in Fig. 3G. Myocardial pathology commonly associated with doxorubicin treatment such as myofibrillar loss and cytoplasmic vacuolisation (Chatterjee et al., 2009) was not observed in the DOX group which could be due to the early stage of the treatment. It should be noted that the DOX group was sacrificed earlier (days 17–18) than the other groups (day 45) due to the significant side effects and mice in this group received only two injections while the other groups were treated six times. Liver damage was evident in the DOX group i.e. there was a loss of blood sinusoid and the development of fatty droplets (Fig. 3G). Clear changes in spleen tissue histology were also observed with fewer white pulp areas (the blue staining represents lymphocytes) seen in the cross-sections. In contrast, mice receiving DPEG-CaFe-TOPSi or DPEG-DOX-CaFe-TOPSi did not differ from the control group in the histology of the examined vital organs. Overall, the serum biochemistry and histopathological analyses indicate that free DOX evoked toxicity in the mice while DPEG-CaFe-TOPSi and DPEG-DOX-CaFe-TOPSi were safe at these doses. As a summary, the loading of DOX inside of the nanoparticle was able to nullify the toxic effects evoked by free DOX, a phenomenon attributed to the pH-controlled drug release.

To further evaluate the possibility that the nanovectors could be utilized in MRI-based monitoring, the liver and lungs from the control, DPEG-CaFe-TOPSi and DPEG-DOX-CaFe-TOPSi groups were imaged. $R_2$ relaxivity was determined in order to detect possible differences since iron is known to increase $R_2$ values. The liver and lung $R_2$ values were significantly elevated in DPEG-CaFe-TOPSi and slightly increased in DPEG-DOX-CaFe-TOPSi group as compared to the control group, indicating the presence of nanoparticles (Fig. S19 and Table S3). Therefore, after their intravenous administration, these particles display properties which can be utilized in MRI diagnostics (Nissinen et al., 2016).

The *in vivo* antitumor efficacy was evaluated with subcutaneous CT26 tumor bearing female BALB/c nude mice which had received a single intratumoral injection. The treatment was conducted when the tumors reached 0.2 cm in diameter (day 7 after tumor inoculation). The body weights of the mice were evaluated every second day until the mice were sacrificed at day 10 post-injection (Fig. 4A). The mice in the control, DPEG-CaFe-TOPSi or DPEG-DOX-CaFe-TOPSi groups did not show any weight differences but the mice in the DOX group started to lose weight 4 days p.i, an effect associated with DOX's toxicity. Furthermore, one mouse in the DOX group died during the monitoring period (at day 8 p.i.) further highlighting the adverse effect of the cytostatic drug treatment. The tumor volumes increased steadily in the control and DPEG-CaFe-TOPSi groups throughout the whole experiment period (Fig. 4B). However, smaller tumor volumes were observed 6 day p.i. in DOX and DPEG-DOX-CaFe-TOPSi groups, and at 10 day p.i. the measured tumor volumes in DOX and DPEG-DOX-CaFe-TOPSi group were significantly smaller than in the other groups (Fig. 4B).

The tumors were weighed at the end of the experiment and showed similar results (Fig. 4C); the tumors in the DOX and DPEG-DOX-CaFe-TOPSi groups were significantly lighter and smaller than those in the control group while no significant difference was detected in the group receiving DPEG-CaFe-TOPSi (Fig. 4D). Comparable and significant tumor size reductions were observed in the DPEG-DOX-CaFe-TOPSi (77%) and DOX (81%) treated tumors, evidence of an excellent therapeutic response. Furthermore, the level of apoptosis was evaluated in tumors with the TUNEL assay. In agreement with our *in vivo* antitumor efficacy results, the tumors dissected from DOX and DPEG-DOX-CaFe-TOPSi groups exhibited similar levels of TUNEL-positive cells indicative of apoptosis (brown colour) (Han et al., 2017); their numbers were clearly higher than the corresponding values in the control and DPEG-CaFe-TOPSi groups (Fig. 4E). Furthermore, the toxicity towards vital organs was evaluated with H&E staining (Fig. S20). In comparison with the control group, the DOX group showed significant lesions in liver, spleen and lung although the drug had been administered only 10 days earlier. Hepatonecrosis had occurred and there were obvious lesions in the splenic germinal center in the DOX group. Moreover, some pulmonary fibrosis could be observed in the DOX group. In contrast, the mice in the other groups did not develop any significant organ lesions, indicating that the free DOX alone causes severe toxicity while the nanoparticles and the DOX loaded nanoparticles seem to be safe. These results suggest that the nanovectors were able to retain the drug more efficiently in the tumor while free drug was escaping the tumor environment, causing toxic effects and damaging vital organs.

## 4. Conclusions

The designed magnetic pH-responsive nanovectors based on porous silicon nanoparticles exhibited good magnetic behaviour, excellent colloidal stability and pH-sensitive drug release *in vitro* and displayed effective therapeutic efficacy. The drug loaded nanovectors did not cause any adverse side effects after systemic administration, being apparently safe over a relatively long time-scale (45 days) and were detectable with MRI *ex vivo*. Furthermore, the nanovectors exhibited a comparable therapeutic response *in vivo* as with free drug but without inducing similar unwanted effects. Therefore, these novel multifunctional PSi nanovectors are very promising candidates and may represent next generation nanomedicines for cancer therapy.

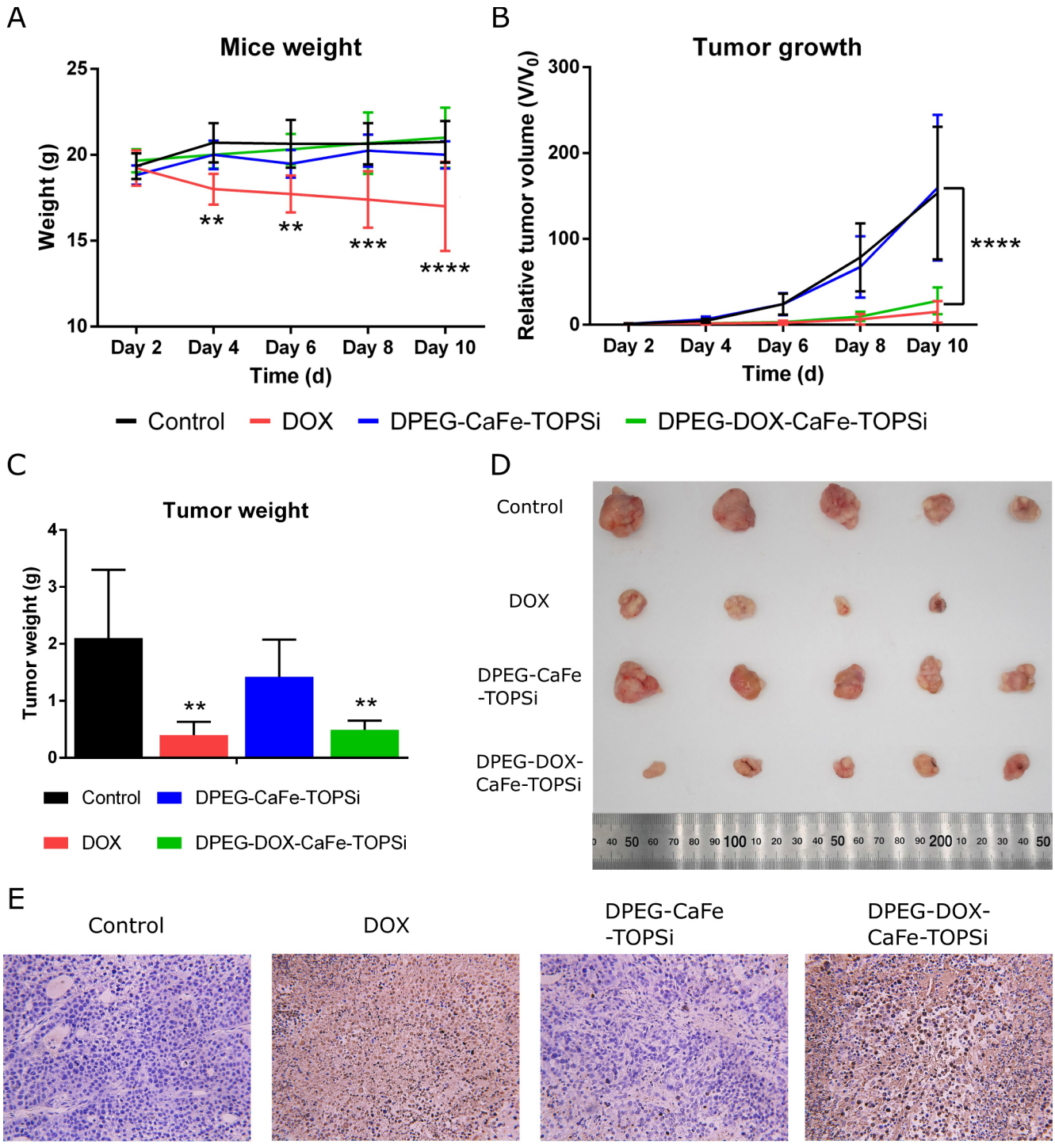


**Fig. 4.** A) Body weight of CT26 bearing BALB/c mice post-injection. The mice were treated with a single intravenous injection of PBS, DOX (5 mg/kg), DPEG-CaFe-TOPSi (50 mg/kg) or DPEG-DOX-CaFe-TOPSi (50 mg/kg, DOX equivalent 5 mg/kg) at day 0. B) Relative tumor growth progression during the 10 day experiment. B) The tumor volume growth progression curves for CT26 tumors during the 10 day period of the experiment. C) Tumor weights 10 d p.i. D) Tumors collected from mice at the end of the experiment (day 10). E) TUNEL assay of tumor biopsies from all treatment groups. Images were randomly taken at 200× magnification for each specimen. Results are presented as mean ± S.D. (n = 5) except for the DOX group where one animal died on day 8 after treatment. Significant differences (compared to the control group (black)) were examined using two-way ANOVA followed by Sidak's test (A&B) and one-way ANOVA followed by Tukey's test (C) (**p < 0.01, ****p < 0.0001).

## 5. Disclosure statement

The authors declare no conflict of interest.

## Acknowledgements

S. Näkki, V.-P. Lehto and W. Xu acknowledge Academy of Finland (grant nos. 314412 and 314552), University of Eastern Finland, Magnus Ehrnrooth Foundation, North-Savo regional fund, Cancer Foundation, Olvi Foundation and Kuopio University Foundation for financial support. L. Fan acknowledges funding from the National Natural Science Foundation of China No. 81201179, the National Key Research and Development Program of China (2017YFC0107405), Natural Science Basic Research Plan in Shaanxi Province of China (2017JQ8049) and

State Key Laboratory of Cancer Biology Open Fund (CBSKL201706). K. Al-Jamal acknowledges funding from Worldwide Cancer Research (12-1054). Sirpa Peräniemi is acknowledged for her assistance with the AAS measurements.

## Appendix A. Supplementary data

Supplementary data to this article can be found online at https://doi.org/10.1016/j.ijpharm.2018.10.074.

## References


Bao, G., Mitragotri, S., Tong, S., 2013. Multifunctional nanoparticles for drug delivery and molecular imaging. Annu. Rev. Biomed. Eng. 15, 253–282. https://doi.org/10.1146/annurev-bioeng-071812-152409.

Barenholz, Y., 2012. Doxil® — the first FDA-approved nano-drug: lessons learned. J. Controlled Release 160, 117–134. https://doi.org/10.1016/j.jconrel.2012.03.020.

Beik, J., Abed, Z., Ghoreishi, F.S., Hosseini-Nami, S., Mehrzadi, S., Shakeri-Zadeh, A., Kamrava, S.K., 2016. Nanotechnology in hyperthermia cancer therapy: from fundamental principles to advanced applications. J. Controlled Release 235, 205–221. https://doi.org/10.1016/j.jconrel.2016.05.062.

Cai, X., Jia, X., Gao, W., Zhang, K., Ma, M., Wang, S., Zheng, Y., Shi, J., Chen, H., 2015. A versatile nanotheranostic agent for efficient dual-mode imaging guided synergistic chemo-thermal tumor therapy. Adv. Funct. Mater. 25, 2520–2529. https://doi.org/10.1002/adfm.201403991.

Canham, L.T., 1995. Bioactive silicon structure fabrication through nanoetching techniques. Adv. Mater. 7, 1033–1037. https://doi.org/10.1002/adma.19950071215.

Chatterjee, K., Zhang, J., Honbo, N., Karliner, J.S., 2009. Doxorubicin cardiomyopathy. Cardiology 115, 155–162. https://doi.org/10.1159/000265166.

Cheng, Y., Morshed, R.A., Auffinger, B., Tobias, A.L., Lesniak, M.S., 2014. Multifunctional nanoparticles for brain tumor imaging and therapy. Adv. Drug Deliv. Rev. 66, 42–57. https://doi.org/10.1016/j.addr.2013.09.006.

Cole, J.T., Holland, N.B., 2015. Multifunctional nanoparticles for use in theranostic applications. Drug Deliv. Transl. Res. 5, 295–309. https://doi.org/10.1007/s13346-015-0218-2.

Gallagher, F.A., Kettunen, M.I., Day, S.E., Hu, D., Ardenkjaer-Larsen, J., Zandt, R.I., Jensen, P.R., Karlsson, M., Golman, K., Lerche, M.H., Brindle, K.M., 2008. Magnetic resonance imaging of pH in vivo using hyperpolarized 13C-labelled bicarbonate. Nature 453, 940–943. https://doi.org/10.1038/nature07017.

Han, L., Tang, C., Yin, C., 2016. pH-Responsive core-shell structured nanoparticles for triple-stage targeted delivery of doxorubicin to tumors. ACS Appl. Mater. Interfaces 8, 23498–23508. https://doi.org/10.1021/acsami.6b07173.

Han, H., Valdeperez, D., Jin, Q., Yang, B., Li, Z., Wu, Y., Pelaz, B., Parak, W.J., Ji, J., 2017. Dual enzymatic reaction-assisted gemcitabine delivery systems for programmed pancreatic cancer therapy. ACS Nano 11, 1281–1291. https://doi.org/10.1021/acsnano.6b05541.

He, Q., Zhang, Z., Gao, F., Li, Y., Shi, J., 2011. In vivo biodistribution and urinary excretion of mesoporous silica nanoparticles: effects of particle Size and PEGylation. Small 7, 271–280. https://doi.org/10.1002/smll.201001459.

Janib, S.M., Moses, A.S., MacKay, J.A., 2010. Imaging and drug delivery using theranostic nanoparticles. Adv. Drug Deliv. Rev. 62, 1052–1063. https://doi.org/10.1016/j.addr.2010.08.004.

Jia, F., Liu, X., Li, L., Mallapragada, S., Narasimhan, B., Wang, Q., 2013. Multifunctional nanoparticles for targeted delivery of immune activating and cancer therapeutic agents. J. Controlled Release 172, 1020–1034. https://doi.org/10.1016/j.jconrel.2013.10.012.

Kinsella, J.M., Ananda, S., Andrew, J.S., Grondek, J.F., Chien, M., Scadeng, M., Gianneschi, N.C., Ruoslahti, E., Sailor, M.J., 2011. Enhanced magnetic resonance contrast of Fe3O4 nanoparticles trapped in a porous silicon nanoparticle host. Adv. Mater. 23, H248–H253. https://doi.org/10.1002/adma.201101877.

Kramer, L., Winter, G., Baur, B., Kuntz, A.J., Kull, T., Solbach, C., Beer, A.J., Linden, M., 2017. Quantitative and correlative biodistribution analysis of Zr-89-labeled mesoporous silica nanoparticles intravenously injected into tumor-bearing mice. Nanoscale 9, 9743–9753. https://doi.org/10.1039/c7nr02050c.

Laubrock, N., Hempel, G., Schulze-Westhoff, P., Würthwein, G., Flege, S., Boos, J., 2000. The stability of doxorubicin and idarubicin in plasma and whole blood. Chromatographia 52, 9–13. https://doi.org/10.1007/BF02490784.

Liang, P., Zhao, D., Wang, C., Zong, J., Zhuo, R., Cheng, S., 2013. Facile preparation of Heparin/CaCO3/CaP hybrid nano-carriers with controllable size for anticancer drug delivery. Colloids Surf. B 102, 783–788. https://doi.org/10.1016/j.colsurfb.2012.08.056.

Liang, P., Chen, Y., Chiang, C., Mo, L., Wei, S., Hsieh, W., Lin, W., 2016. Doxorubicin-modified magnetic nanoparticles as a drug delivery system for magnetic resonance imaging-monitoring magnet-enhancing tumor chemotherapy. Int. J. Nanomed. 11, 2021–2037. https://doi.org/10.2147/IJN.S94139.

Liu, J., Luo, Z., Zhang, J., Luo, T., Zhou, J., Zhao, X., Cai, K., 2016. Hollow mesoporous silica nanoparticles facilitated drug delivery via cascade pH stimuli in tumor microenvironment for tumor therapy. Biomaterials 83, 51–65. https://doi.org/10.1016/j.biomaterials.2016.01.008.

Liu, Y., Zhi, X., Yang, M., Zhang, J., Lin, L., Zhao, X., Hou, W., Zhang, C., Zhang, Q., Pan, F., Alfranca, G., Yang, Y., de la Fuente, J.M., Ni, J., Cui, D., 2017. Tumor-triggered drug release from calcium carbonate-encapsulated gold nanostars for near-infrared photodynamic/photothermal combination antitumor therapy. Theranostics 7, 1650–1662. https://doi.org/10.7150/thno.17602.

Lu, M., Merali, S., Gordon, R., Jiang, J., Li, Y., Mandeli, J., Duan, X., Fallon, J., Holland, J.F., 2011. Prevention of doxorubicin cardiopathic changes by a benzyl styryl sulfone in mice. Genes Cancer 2, 985–992. https://doi.org/10.1177/1947601911436199.

Nissinen, T., Näkki, S., Laakso, H., Kučiauskas, D., Kaupinis, A., Kettunen, M.I., Liimatainen, T., Hyvönen, M., Valius, M., Gröhn, O., Lehto, V., 2016. Tailored Dual PEGylation of inorganic porous nanocarriers for extremely long blood circulation in vivo. ACS Appl. Mater. Interfaces 8, 32723–32731. https://doi.org/10.1021/acsami.6b12481.

Näkki, S., Rytkönen, J., Nissinen, T., Florea, C., Riikonen, J., Ek, P., Zhang, H., Santos, H.A., Närvänen, A., Xu, W., Lehto, V., 2015. Improved stability and biocompatibility of nanostructured silicon drug carrier for intravenous administration. Acta Biomater. 13, 207–215. https://doi.org/10.1016/j.actbio.2014.11.019.

Näkki, S., Martinez, J.O., Evangelopoulos, M., Xu, W., Lehto, V., Tasciotti, E., 2017. Chlorin e6 functionalized theranostic multistage nanovectors transported by stem cells for effective photodynamic therapy. ACS Appl. Mater. Interfaces 9, 23441–23449. https://doi.org/10.1021/acsami.7b05766.

Park, J.-H., Gu, L., von Maltzahn, G., Ruoslahti, E., Bhatia, S.N., Sailor, M.J., 2009. Biodegradable luminescent porous silicon nanoparticles for in vivo applications. Nat. Mater. 8, 331–336. https://doi.org/10.1038/NMAT2398.

Parodi, A., Quattrocchi, N., van de Ven, A.L., Chiappini, C., Evangelopoulos, M., Martinez, J.O., Brown, B.S., Khaled, S.Z., Yazdi, I.K., Enzo, M.V., Isenhart, L., Ferrari, M., Tasciotti, E., 2013. Synthetic nanoparticles functionalized with biomimetic leukocyte membranes possess cell-like functions. Nat. Nanotechnol. 8, 61–68. https://doi.org/10.1038/nnano.2012.212.

Russell, L.M., Hultz, M., Searson, P.C., 2018. Leakage kinetics of the liposomal chemotherapeutic agent Doxil: the role of dissolution, protonation, and passive transport, and implications for mechanism of action. J. Controlled Release 269, 171–176. https://doi.org/10.1016/j.jconrel.2017.11.007.

Rytkönen, J., Miettinen, R., Kaasalainen, M., Lehto, V., Salonen, J., Närvänen, A., 2012. Functionalization of mesoporous silicon nanoparticles for targeting and bioimaging purposes. J. Nanomater. 896562. https://doi.org/10.1155/2012/896562.

Salonen, J., Kaukonen, A.M., Hirvonen, J., Lehto, V., 2008. Mesoporous silicon in drug delivery applications. J. Pharm. Sci. 97, 632–653. https://doi.org/10.1002/jps.20999.

Shi, J., Kantoff, P.W., Wooster, R., Farokhzad, O.C., 2017. Cancer nanomedicine: progress, challenges and opportunities. Nat. Rev. Cancer 17, 20–37. https://doi.org/10.1038/nrc.2016.108.

Shultz, L.D., Ishikawa, F., Greiner, D.L., 2007. Humanized mice in translational biomedical research. Nat. Rev. Immunol. 7, 118. https://doi.org/10.1038/nri2017.

Sun, C., Liu, Y., Du, J., Cao, Z., Xu, C., Wang, J., 2016. Facile generation of tumor-pH-labile linkage-bridged block copolymers for chemotherapeutic delivery. Angew. Chem. Int. Ed. 55, 1010–1014. https://doi.org/10.1002/anie.201509507.

Takemura, G., Fujiwara, H., 2007. Doxorubicin-induced cardiomyopathy. Progr. Cardiovasc. Dis. 49, 330–352. https://doi.org/10.1016/j.pcad.2006.10.002.

Tölli, M.A., Ferreira, M.P.A., Kinnunen, S.M., Rysä, J., Mäkilä, E.M., Szabó, Z., Serpi, R.E., Ohukainen, P.J., Välimäki, M.J., Correia, A.M.R., Salonen, J.J., Hirvonen, J.T., Ruskoaho, H.J., Santos, H.A., 2014. In vivo biocompatibility of porous silicon biomaterials for drug delivery to the heart. Biomaterials 35, 8394–8405. https://doi.org/10.1016/j.biomaterials.2014.05.078.

Wang, Y., Zhao, R., Wang, S., Liu, Z., Tang, R., 2016. In vivo dual-targeted chemotherapy of drug resistant cancer by rationally designed nanocarrier. Biomaterials 75, 71–81. https://doi.org/10.1016/j.biomaterials.2015.09.030.

Wei, W., Ma, G., Hu, G., Yu, D., Mcleish, T., Su, Z., Shen, Z., 2008. Preparation of hierarchical hollow CaCO3 particles and the application as anticancer drug carrier. J. Am. Chem. Soc. 130, 15808–15810. https://doi.org/10.1021/ja8039585.

Wu, R., Wang, H., Yu, H., Cui, X., Xu, M., Xu, X., Gao, J., 2016. Doxorubicin toxicity changes myocardial energy metabolism in rats. Chem. Biol. Interact. 244, 149–158. https://doi.org/10.1016/j.cbi.2015.12.010.

Xia, B., Li, J., Shi, J., Zhang, Y., Zhang, Q., Chen, Z., Wang, B., 2017. Biodegradable and magnetic-fluorescent porous silicon@Iron oxide nanocomposites for fluorescence/magnetic resonance bimodal imaging of tumor in vivo. ACS Biomater. Sci. Eng. 3, 2579–2587. https://doi.org/10.1021/acsbiomaterials.7b00467.

Xie, J., Lee, S., Chen, X., 2010. Nanoparticle-based theranostic agents. Adv. Drug Deliv. Rev. 62, 1064–1079. https://doi.org/10.1016/j.addr.2010.07.009.

Yang, S., Chen, D., Li, N., Xu, Q., Li, H., Gu, F., Xie, J., Lu, J., 2016. Hollow mesoporous silica nanocarriers with multifunctional capping agents for in vivo cancer imaging and therapy. Small 12, 360–370. https://doi.org/10.1002/smll.201503121.

Zhang, Q., Wang, X., Li, P., Nguyen, Kim Truc, Wang, X., Luo, Z., Zhang, H., Tan, N.S., Zhao, Y., 2014. Biocompatible, uniform, and redispersible mesoporous silica nanoparticles for cancer- targeted drug delivery in vivo. Adv. Funct. Mater. 24, 2450–2461. https://doi.org/10.1002/adfm.201302988.

Zhang, W., Wang, G., Falconer, J.R., Baguley, B.C., Shaw, J.P., Liu, J., Xu, H., See, E., Sun, J., Aa, J., Wu, Z., 2015. Strategies to maximize liposomal drug loading for a poorly water-soluble anticancer drug. Pharm. Res. 32, 1451–1461. https://doi.org/10.1007/s11095-014-1551-8.

Zhao, P., Li, M., Wang, Y., Chen, Y., He, C., Zhang, X., Yang, T., Lu, Y., You, J., Lee, R.J., Xiang, G., 2018. Enhancing anti-tumor efficiency in hepatocellular carcinoma through the autophagy inhibition by miR-375/sorafenib in lipid-coated calcium carbonate nanoparticles. Acta Biomater. 72, 248–255. https://doi.org/10.1016/j.actbio.2018.03.022.